ADVANCED MATERIALS
www.advmat.de

Carrier-Transport Mechanism in Organic Antiambipolar Transistors Unveiled by Operando Photoemission Electron Microscopy

Ryoma Hayakawa, Soichiro Takeiri, Yoichi Yamada, Yutaka Wakayama, and Keiki Fukumoto**

Organic antiambipolar transistors (AATs) have partially overlapped p–n junctions. At room temperature, this p–n junction induces a negative differential transconductance in an AAT. However, the detailed carrier-transport mechanism remains unclear. Herein, an operando photoemission electron microscopy is used to tackle this issue owing to the technique's ability to visualize conductive electrons in real time during transistor operation. Notably, it is observed that when the AAT is on, a depletion layer forms at the lateral p–n junction. The visualized depletion layer shows that both p- and n-type channels have pinch-off states in the gate voltage range when the AAT is in on state. The steep potential gradient at the lateral p–n interface enhances the electron conduction from n-type to p-type semiconductor. Another significant finding is that most electrons are considered to recombine with the accumulated holes in the p-type semiconductor, affording the reduction of photoemission intensity by ≈80%. This technique provides a thorough understanding of carrier transport in AATs, further improving the device performance.

1. Introduction

Considerable efforts have been devoted to the development of antiambipolar transistors (AATs).[1–8] A unique characteristic of AATs is that the p-type and n-type semiconductor films partially overlap in the transistor channel to form p–n junctions. As shown in **Figure 1**a, the AAT has two p–n junctions in the vertical and lateral directions in the partially overlapped region. This structural feature enables a Λ-shaped transfer curve; a negative differential transconductance (NDT) is visible above a certain gate bias voltage (V_{peak}). With the monotonical increase in the gate voltage, the drain current rapidly increases and then decreases. Similar Λ-shaped transfer curves have been obtained using quantum devices, such as Esaki-tunneling transistors, resonant-tunneling transistors, and single-carrier transistors.[9–13] However, the operation of these devices has been limited at cryogenic temperatures. Conversely, the AATs exhibit NDT even at room temperature; thus, the AATs are in the spotlight for the development of new computing architectures.

Nowadays, various types of materials, including 2D materials[1–3] and a combination of inorganic and organic materials,[4–6] have been used as transistor channels to enhance the AAT device performance. For example, a low operation voltage <1 V has already been achieved.[2] A typical application of the AATs is in multivalued logic (MVL) circuits. MVL circuits exhibit high data processing capability, low power consumption, and a large-scale integration compared to conventional binary logic circuits. The MVL circuits, including ternary and quaternary inverters, were realized using a unique transport property of AATs.[2,14–16] In another case, electrically reconfigurable logic circuits, such as the electrical switching of binary and ternary inverter operations, have been demonstrated.[17] Such device operations are unavailable when using the current complementary metal–oxide–semiconductor (CMOS) inverters. Thus, the development of AATs holds promise for the upcoming big-data era.

We proposed using organic p- and n-type semiconductors as transistor channels due to the following advantages: high controllability of energy levels by external fields, mechanical flexibility, and facile processability of organic materials.[18–28] Thus far, we have achieved considerably high gate tunability of the drain currents in organic AATs.[18–20] The ratio of the peak- and off-drain currents reached four orders of magnitude. These transistors helped demonstrate ternary inverter operations by combining with *n*-type transistors.[21,22,24] Another advantage of organic materials is their high photoresponsivity, which allows optical control of the ternary inverters.[26] Currently, the concept

R. Hayakawa, S. Takeiri, Y. Wakayama
International Center for Materials Nanoarchitectonics (WPI-MANA)
National Institute for Materials Science (NIMS)
1-1 Namiki, Tsukuba, Ibaraki 305-0044, Japan
E-mail: wakayama.yutaka@nims.go.jp
S. Takeiri, Y. Yamada
Institute of Pure and Applied Sciences
University of Tsukuba
1-1-1 Tennodai, Tsukuba, Ibaraki 305-8573, Japan
K. Fukumoto
High Energy Accelerator Research Organization (KEK)
1-1 Oho, Tsukuba, Ibaraki 305-0801, Japan
E-mail: keiki@post.kek.jp
The ORCID identification number(s) for the author(s) of this article can be found under https://doi.org/10.1002/adma.202201277.

DOI: 10.1002/adma.202201277

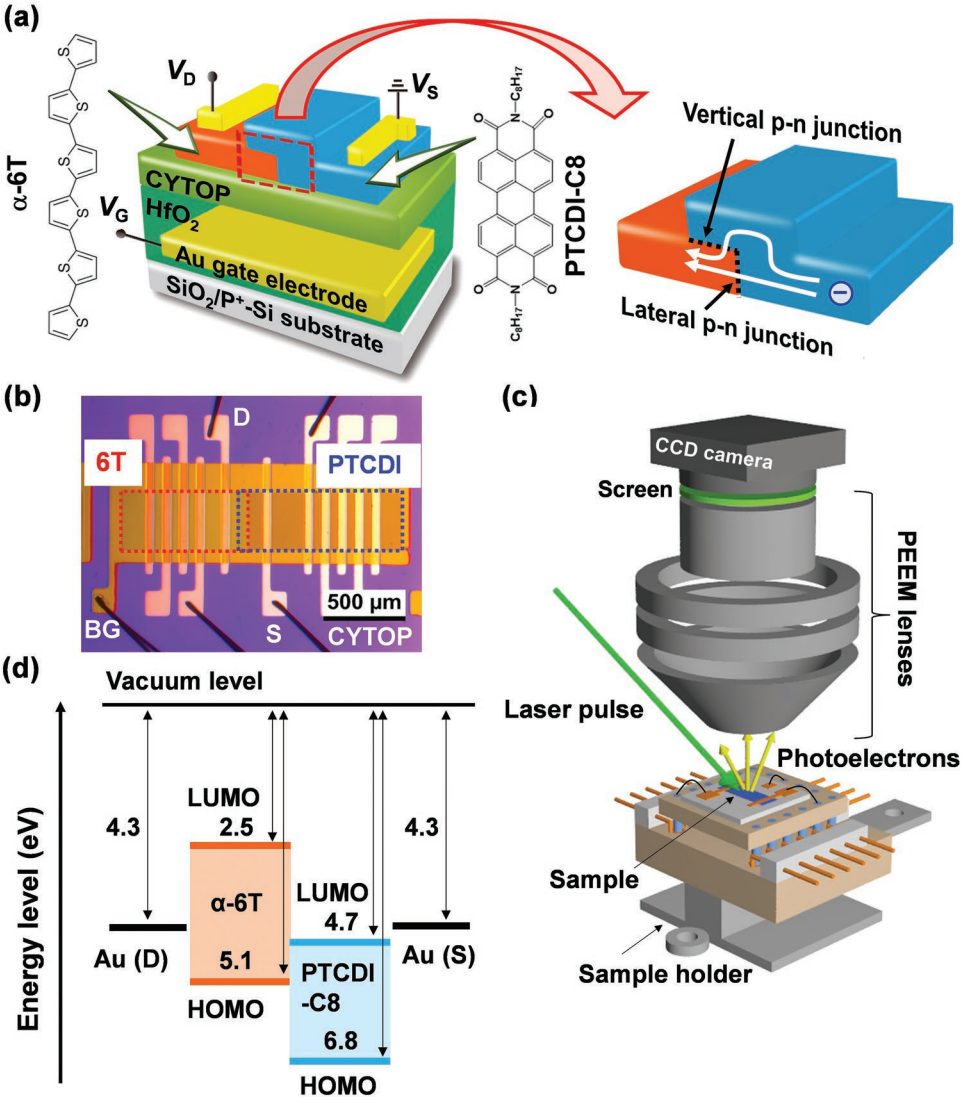

Figure 1. a) Device structure with enlarged drawing to show the vertical and lateral p–n junctions. b) Optical microscopy image of an antiambipolar transistor (AAT) with α-6T and PTCDI-C8 channel layers. c) Photoemission electron microscopy (PEEM) measurement experimental setup. d) Energy-level alignment of the source–drain electrodes (Au), α-6T, and PTCDI-C8 channel layers. The highest occupied molecular orbital (HOMO) and lowest unoccupied molecular orbital (LUMO) levels of both layers were determined using the photoelectron emission spectroscopy measurements.

of optically controllable MVL circuits is expanded to flexible applications.[27,28] We have achieved optically tunable ternary inverter operations with well-balanced output signals and extremely high bending endurance on flexible substrates.[27]

Organic AATs are crucial for the development of new application platforms. However, the carrier-transport mechanism remains unclear although the transport has been explained in analogy with a shoot-through current (STC) in a CMOS inverter.[18–25] Thus, revealing the carrier-transport mechanism is a critical issue to clarify the origin of the NDT and improve the device's performance. Herein, we use operando photoemission electron microscopy (PEEM) to tackle this issue. This technique can visualize the spatial distribution of the electrons under actual transistor operation.[29–33] Furthermore, we can directly examine the manner in which electrons flow in the transistor channels. The PEEM analyses revealed that electrons were injected from the source electrode into the n-type semiconductor; subsequently, they were transported to the p-type semiconductor in the case of n-type operation. Importantly, the pinch-off state in the constituent channels induced the formation of a depletion layer at the lateral p–n junction, indicating that the electrons flow through the lateral p–n junction. Additionally, most electrons recombined with the accumulated holes in the p-type semiconductor. These findings give us a better understanding of the carrier transport in AATs and a hint for achieving high-performance organic AATs.

2. Results and Discussion

Figure 1a,b presents the device structure and the optical microscopy image of the organic AAT. The transistor has

a bottom-gate (BG) and a top-contact (TC) configuration, where α-sexithiophene (α-6T) and *N,N′*-dioctyl-3,4,9,10-perylenedicarboximide (PTCDI-C8) are used as p-type and n-type transistor channels, respectively. Conductive electrons accumulate near the gate insulator/channel interface. To detect such conductive electrons using PEEM measurement, the film thickness was reduced to 10 nm for the α-6T layer and 15 nm for the PTCDI-C8 layer (Figure 1c). As shown in Figure S1 (Supporting Information), atomic force microscopy images confirmed that both the channel layers and the partially stacked p–n region have smooth surface morphologies. The work function of Au and the energy levels of the molecular orbitals of α-6T and PTCDI-C8 were examined using photoelectron emission spectroscopy. Figure 1d shows the estimated energy-level alignment with respect to the vacuum level. The energy levels of the highest occupied molecular orbital (HOMO) and the lowest unoccupied molecular orbital (LUMO) were estimated to be 5.1 and 2.5 eV for the α-6T film and 6.8 and 4.7 eV for the PTCDI-C8 film, respectively. The detailed estimation process is given in the Figures S2 and S3 (Supporting Information). These energy levels of the molecular orbitals are in agreement with those reported previously.[18,34–36] The work function of Au was 4.3 eV, which is similar to those measured under atmospheric conditions.[37,38] Importantly, the energy-level alignment has a type-II configuration in the absence of bias voltages. Namely, the LUMO level of the PTCDI-C8 film is located between the HOMO and LUMO levels of the α-6T film.

We first investigated the fundamental transistor properties of the organic AAT. **Figure 2**a ,b shows the drain current (I_D)-gate voltage (V_G) curve and the differential transconductance ($g_m = dI_D/dV_G$) curve in the case of *n*-type operation, where the drain voltage (V_D) was fixed at 10 V. The channel width and length were 400 µm and 200 µm, respectively. The AAT showed a typical Λ-shaped transfer curve (Figure 2a). The I_D started increasing at V_G (= V_{on}) = 2.6 V and then reached the maximum peak drain current (I_{peak} = 18.8 nA) at V_G (= V_{peak}) = 3.6 V. Further increase in V_G dropped I_D and the transistor became off state at V_G (= V_{off}) = 6.6 V. Figure 2b shows the corresponding NDT. The minimum value of NDT, g_{min}, was obtained as –16 nS at V_G = 3.7 V.

The Λ-shaped transfer curve, namely NDT characteristics, is induced via same mechanism as that of STC in the CMOS inverter[18–25] because the equivalent circuit of an AAT is defined as a series circuit of n-type and p-type transistors (the inset of Figure 2c). The I_D is represented as the overlapped current of two transfer curves in the saturation region of the α-6T and PTCDI-C8 transistors, where the p–n junction can be regarded as a common "quasidrain electrode" of α-6T and PTCDI-C8 transistors. To validate the model, we analyzed the AAT's I_D–V_G curve using the following equations:[25]

$$I_{D,n} = \frac{W}{2L_n}\mu_n C_i (V_G - V_{th,n})^2 \quad (1)$$

$$I_{D,p} = \frac{W}{2L_p}\mu_p C_i (V_D - V_G + V_{th,p})^2 \quad (2)$$

where L_n and L_p are the effective channel lengths of the PTCDI-C8 and α-6T channels (in this case, 100 µm for both channels), W is the common channel width (400 µm), and C_i is the capacitance of the insulator per unit area (73.5 nF cm^{-1}). $I_{D,n}$, μ_n, and $V_{th,n}$ are the PTCDI-C8 transistor's I_D in the saturation region, electron carrier mobility, and threshold voltage, respectively.

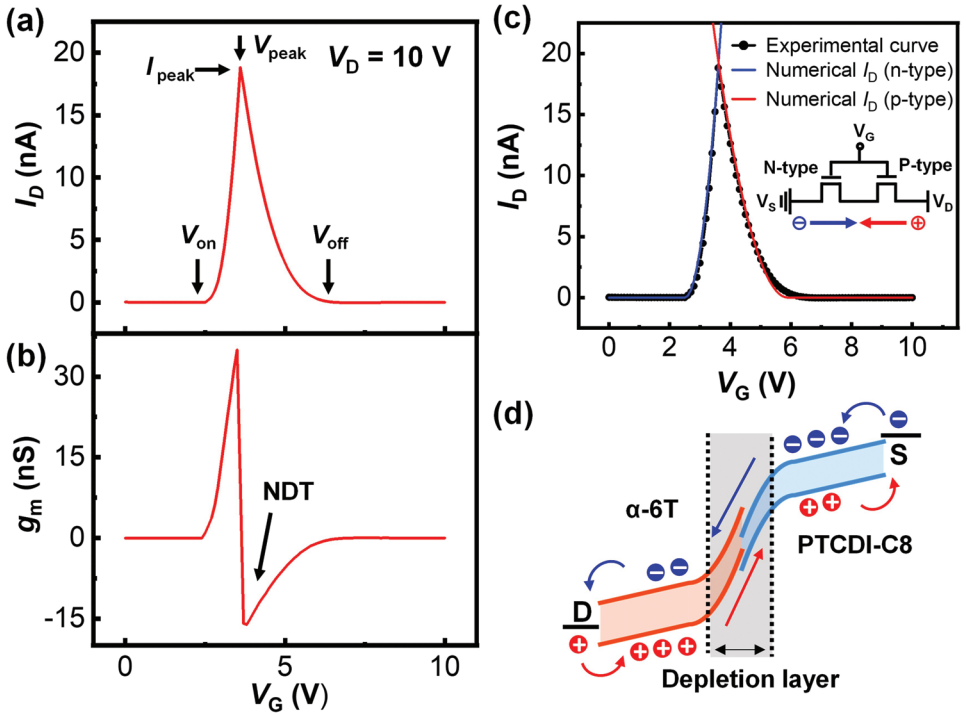

Figure 2. a) I_D–V_G curve and b) the corresponding differential transconductance curve of the AAT in the n-type operation. c) Comparison of the experimental and numerical I_D–V_G curves. d) Energy-level alignment inferred from the analysis of the transfer curve shown in (c).

$I_{D,p}$, μ_p, and $V_{th,p}$ are the α-6T transistor's I_D in the saturation region, hole carrier mobility, and threshold voltage, respectively. Notably, V_G is directly applied to the PTCDI-C8 channel. However, the voltage difference between V_D and V_G (V_D–V_G) is applied to the α-6T channel as the actual gate bias in the series circuit.

As shown in Figure 2c, the I_D–V_G curve of the AAT was well fitted with the following parameters: $\mu_n = 1.4 \times 10^{-1}$ cm^2 V^{-1} s^{-1}, $V_{th,n} = 2.5$ V, $\mu_p = 3.3 \times 10^{-2}$ cm^2 V^{-1} s^{-1}, and $V_{th,p} = -4.1$ V. These parameters are almost as same as those of the respective transistors (PTCDI-C8 and α-6T transistors) (see Figure S4 and Table S1, Supporting Information). The result shows that the I_D of the AAT is explained as the overlapped current of the two transfer curves in the "saturation region" of the α-6T and PTCDI-C8 transistors. Therefore, both constituent channels are considered to accompany the pinch-off states in the applied V_G and V_D conditions near the p–n junction. This is because the junction behaves as a quasi-drain electrode for both the constituent transistors. This finding implies the formation of a depletion layer at the p–n junction. Based on the above analysis, the energy-level alignment in the $V_{on} < V_G < V_{off}$ range is inferred as shown in Figure 2d, given the applied V_D (= 10 V) and the HOMO–LUMO gaps of the PTCDI-C8 and α-6T films.

Operando PEEM measurements were then conducted under the transistor operation to reveal the detailed carrier-transport process. **Figure 3**a shows the AAT's I_D–V_G curve under the PEEM observation, where V_D was fixed at 12 V. A Λ-shaped transfer curve similar to that in Figure 2a was observed. However, the obtained I_{peak} was 3.3 nA, which was lower than the value in Figure 2a (18.8 nA). The reduction in I_{peak} is caused by the degradation in carrier mobilities under a laser pulse irradiation. Meanwhile, V_{on}, V_{peak}, and V_{off} were calculated to be 1.2, 3.2, and 6.2 V, respectively. These key parameters are close to those obtained from Figure 2a. Therefore, we consider that the fundamental transport process is still maintained throughout the PEEM measurements.

Figure 3b–e shows the PEEM images obtained at different V_G values indicated by blue arrows in Figure 3a. To detect the conductive electrons in the LUMO levels of the channel layers in the AAT (4.7 eV for PTCDI-C8 and 2.5 eV for α-6T, as shown in Figure 1d), the photon energy of the femtosecond laser pulse was fixed at 4.7 eV. However, the electrons in the HOMO levels cannot be observed in this condition because the HOMO levels are located at 6.8 eV for PTCDI-C8 and 5.1 eV for α-6T (Figure 1d). At $V_G = 0$ V, photoemission could not be detected in the PTCDI-C8 and α-6T channels because electrons are not injected into the PTCDI-C8 channel (a depletion layer) and holes are accumulated in the α-6T channel (Figure 3b). Although no electrons are injected from the source electrode, photoemission could be observed in the p–n stacked region. This photoemission is thus attributed to laser-induced electron transfer. The electrons excited from the HOMO level to the LUMO level of the bottom α-6T layer would be transferred to the LUMO level of the top PTCDI-C8 layer. Furthermore, the photoemission intensity from the bright part of the overlapped p–n junction region remained almost constant, even though the I_D values were dependent on the V_G range (Figure 3b–e). These results show that no electrons passed through the vertical p–n junction.

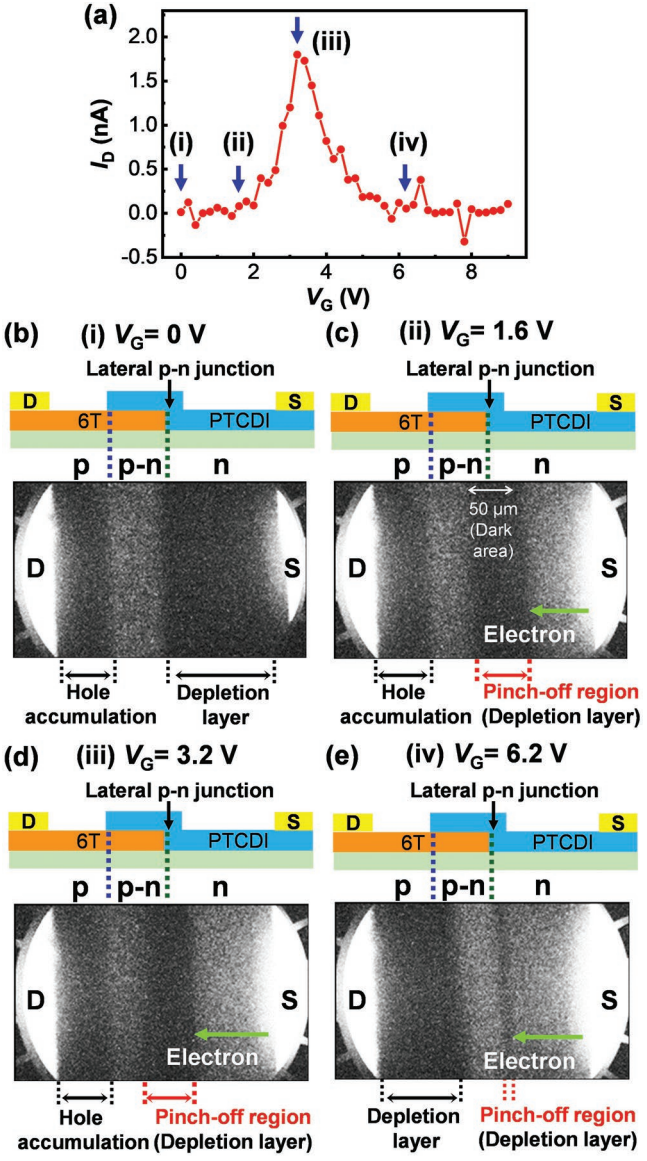

Figure 3. a) I_D–V_G curve of the AAT measured under operando PEEM observation. b–e) The PEEM images of the AAT measured at $V_G = 0$ V (b), V_G (> V_{on}) = 1.6 V (c), V_G (V_{peak}) = 3.2 V (d), and V_G (V_{off}) = 6.2 V (e). These are corresponding to the conditions of (i), (ii), (iii), and (iv) as indicated by blue arrows in (a).

The photoemission from the PTCDI-C8 layer was detected in the PEEM image captured at V_G (>V_{on}) = 1.6 V (Figure 3c), indicating that electrons were injected from the source electrode. A dark area (no photoelectron emission region) appeared around the lateral edge junction of the α-6T and PTCDI-C8 layers as shown by the red dotted lines in Figure 3c, even though the drain current started flowing at the V_G condition. The dark area was seen in both regions of the p–n stacked layers and the PTCDI-C8 layer. The dark area's width was estimated to be ≈25 μm for the p–n stacked layers and the PTCDI-C8 layer (50 μm in the total). We confirmed that a similar dark area (≈25 μm) in the PEEM image was observed around the drain electrode in a single PTCDI-C8 transistor in the saturation

region (Figure S5, Supporting Information). We conclude that a depletion layer is formed at the lateral p–n junction in the AAT. This conclusion is consistent with the analysis of the transistor properties (Figure 2c). However, a width of up to 25 µm is too large for the actual depletion layer of the organic channels. Generally, the depletion width in the pinch-off region has been estimated in the range of 1–5 µm in conventional organic transistors by Kelvin probe force microscopy (KPFM) measurements.[39,40] The discrepancy is caused by the difference in the measurement principles of KPFM and PEEM. In PEEM measurements, the depletion width would be overestimated due to the detection limit of the conductive electrons.

I_D was then enhanced by reducing the depletion layer, reaching I_{peak} at V_G (V_{peak}) = 3.2 V (Figure 3d). Further increment in V_G from 3.2 to 6.2 V minimized the width of the depletion layer (Figure 3e). However, no I_D was detected because the α-6T layer channel was fully depleted.

In contrast to the clear photoemission in the PTCDI-C8 layer, the photoemission intensity in the α-6T layer was extremely weak throughout the V_G range (Figure 3b–e). To examine whether electrons are transferred from the LUMO level of PTCDI-C8 to that of the α-6T channel over the lateral p–n junction, we plotted the averaged photoemission intensities of the α-6T and PTCDI-C8 regions as a function of V_G (**Figure 4**a). The intensities were estimated from the rectangular regions in the PEEM image (the right image in Figure 4a). The corresponding I_D–V_G curve is also depicted in the same figure to obtain an insight into the relation of the photoemission intensities in both layers and the total I_D of the AAT. The I_D–V_G curve is duplicated from Figure 3a. We discovered that the photoemission intensity in the PTCDI-C8 region exhibits stepwise behavior in the profile. The photoemission intensity increased in the range of $V_G > V_{on}$ (= 1.2 V) and reached a plateau at V_G = 1.6 V. This corresponds to electron injection into the PTCDI-C8 channel from the source electrode. Notably, the photoemission intensity in the α-6T region started elevating at the same V_{on}. The result shows that the electrons in the LUMO level of the PTCDI-C8 channel are transported to that of the α-6T channel. The more striking point is that the photoemission intensity in the α-6T region is considerably lower than that in the PTCDI-C8 region. We executed the Markov chain Monte Carlo (MCMC) method to statistically estimate the relative change of photoemission intensities in the α-6T and PTCDI-C8 channels during transistor operation.[41] Detailed information

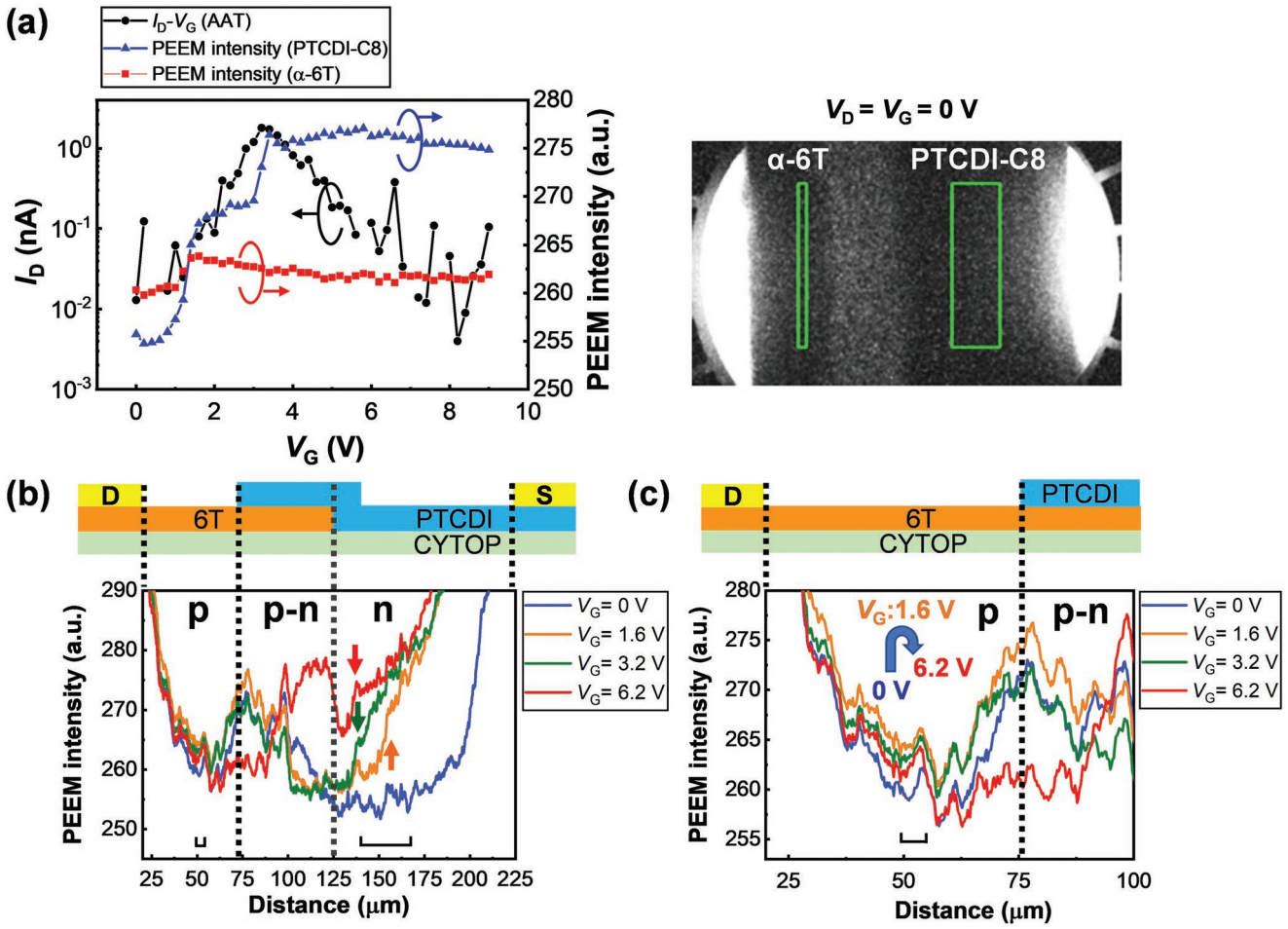

Figure 4. a) I_D–V_G curve of AAT and the averaged photoemission intensities of the α-6T and PTCDI-C8 channel regions as a function of V_G. The photoemission intensities were obtained from the rectangular regions shown in the right PEEM image. b) The photoemission intensity profile in the source to drain electrodes and c) the enlarged profile in the specific area between the p–n stacked region to the drain electrode. Here, V_G was changed from 0 to 6.2 V. The U-shaped black lines shown in (b) and (c) coincide with the widths of the respective rectangular regions shown in the PEEM image of (a).

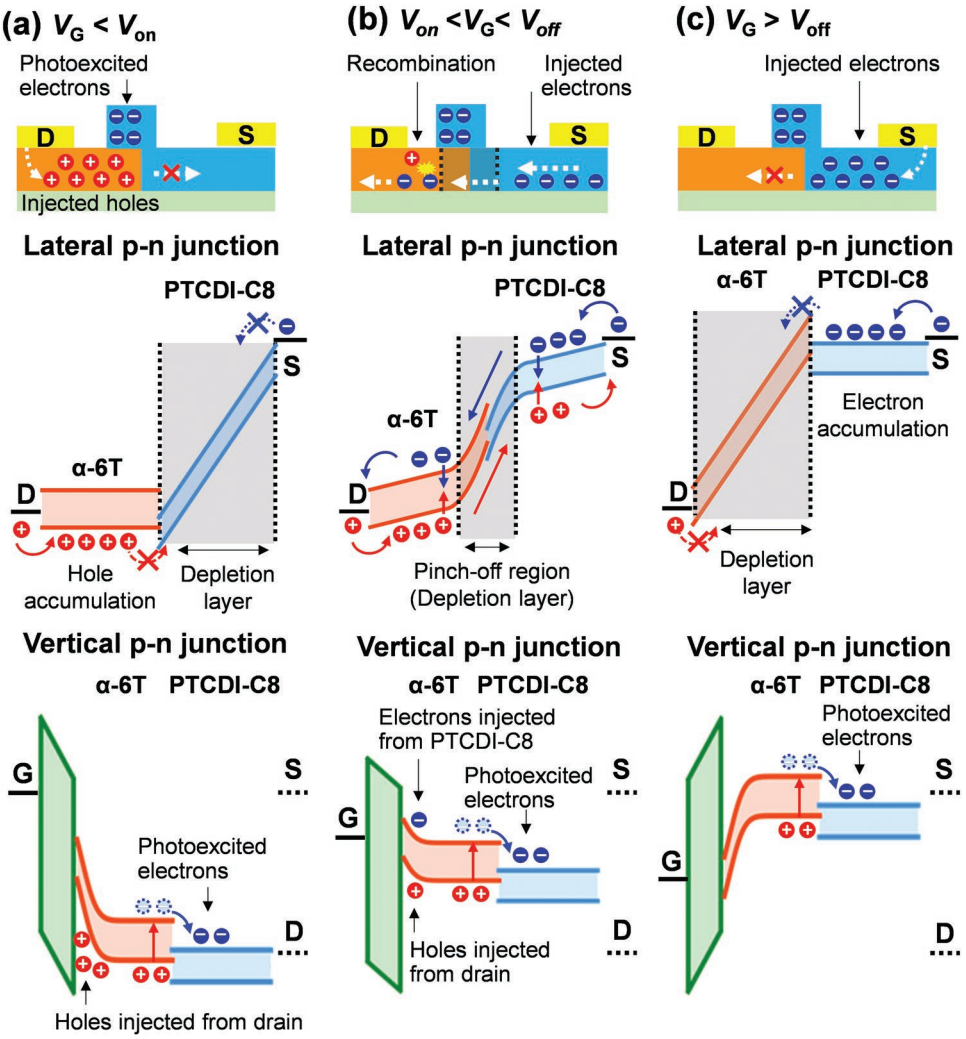

Figure 5. a–c) Illustrations and the energy-level alignments of AAT in the following V_G range: a) $V_G < V_{on}$, b) $V_{on} < V_G < V_{off}$, and c) $V_G > V_{off}$.

regarding this procedure is shown in Figures S6 and S7 (Supporting Information). The statistical analysis revealed that the photoemission intensity was reduced by ≈80% in the α-6T layer, indicating that most electrons recombined with the accumulated holes in the α-6T layer. Similar recombination has been reported in light-emitting transistors with lateral p–n junctions, validating our experimental findings.[42]

Further increase in V_G (V_{peak} > 3.2 V) induced the complete saturation of photoemission intensity in the PTCDI-C8 region. Conversely, the photoemission intensity in the α-6T region gradually decreased in the V_G range due to the transition from accumulation to depletion condition in the α-6T channel.

Figure 4b shows the photoemission intensity profile between the source and drain electrode, which is used to examine the spatial distribution of the electron carriers in the constituent channel layers. With increasing V_G, the electron-injection region in the PTCDI-C8 layer shifted from the edge of the source electrode to the p–n overlapped region, as shown by the arrows in Figure 4b. This result coincides with the variation of the pinch-off region in the PTCDI-C8 channel. However, the photoemission intensity in the α-6T layer entirely increased up to V_G = 1.6 V (Figure 4c). The result shows that the electrons transferred into the α-6T layer are distributed and reach the drain electrode.

Based on the above measurements, the carrier-transport processes in the AAT under the three characteristic V_G ranges ((a) $V_G < V_{on}$, (b) $V_{on} < V_G < V_{off}$, and (c) $V_G > V_{off}$) are summarized in **Figure 5**. The energy-level alignments depend on the direction at the p–n junction: vertical or lateral direction. The difference in the energy-level alignments is caused by the distinct distribution of the applied electric fields (V_G and V_D). In the vertical p–n junction, the applied V_G induced a parallel energetic shift in the HOMO and LUMO levels of both channels, indicating that a drastic energy-level alignment change at the interface of the α-6T and PTCDI-C8 layers does not occur in all V_G ranges. Thus, the vertical p–n junction does not work as the charge-transport path.

Meanwhile, in the lateral direction, the energy-level alignment between the α-6T and PTCDI-C8 layers is varied in accordance with the V_G range, in contrast to the vertical direction. This is because V_D is allocated to the respective channel layers based on the carrier concentrations. When V_G is below V_{on}, the PTCDI-C8 channel is completely depleted because no

electrons are injected from the source electrode (Figure 5a). Conversely, holes are accumulated in the α-6T channel due to the effective gate voltage (V_D–V_G). Therefore, a voltage drop, which coincides with V_D, occurs across the PTCDI-C8 channel in the lateral direction. In this situation, the accumulated holes in the α-6T channel flow to the PTCDI-C8 channel. However, the energy-level offset at the p–n junction disturbs the lateral hole transport. The same explanation applies to those in a high V_G range ($V_G > V_{off}$) (Figure 5c). In this V_G range, I_D is suppressed again because the α-6T layer is completely depleted by the reduction of the gate voltage (V_D–V_G). Even though electrons are accumulated in the PTCDI-C8 channel, the transport to the α-6T layer is hindered by the energy barrier at the lateral p–n interface, similar to the case in $V_G < V_{on}$.

The above situation is largely different in the middle V_G range ($V_{on} < V_G < V_{off}$), where the drain current is flowing (Figure 5b). Our PEEM observation clarifies the presence of a depletion layer at the lateral p–n junction. The result shows that both channel layers have pinch-off states. The marked potential gradient from the PTCDI-C8 to the α-6T channel induces the lateral conduction of electrons. Although the energy-level offset at the p–n junction is considered to be maintained even in the V_G range, as highlighted in our previous theoretical work,[22] the considerable change in the energy-level alignment allows electron conduction via lateral p–n junction.

Another crucial finding is the recombination of minority carriers in the α-6T channel. After the electrons are transported into the α-6T layer, most of them are considered to have recombined with the holes accumulated in the layer. The recombination ratio was estimated to be ≈80% from the difference in the photoelectron intensities of α-6T and PTCDI-C8 layers (Figures S6 and S7, Supporting Information). However, the kinetic energy of the photoelectrons should be considered for more precise estimation.

Finally, we compare the abovementioned carrier-transport mechanism to those in our previous works and other reported ones. In our first report, we proposed that the transport mechanism can be explained using the same analogy as STC in the CMOS inverter.[18] The drain current is determined via accumulation or depletion conditions of the channel layers. Subsequently, we discovered that the carriers flow through the lateral p–n junction rather than the vertical p–n junction.[20] The idea of lateral carrier conduction is also supported by theoretical simulations by Kim et al.[22,23] and Yoo et al.[25] The transport mechanism is further enhanced by Kim et al. They highlighted that the carriers injected from the source electrode are transported via drift conduction in the depleted semiconductor layer. Then, they are conducted by diffusion in the accumulated layer.[23] Furthermore, a moderate energy-level offset can be observed at the lateral p–n junction.[22–25] The offset at the lateral p–n junction is crucial for inducing the off-state in the transistors. Otherwise, the accumulated holes or electrons diffuse to the opposite-side electrode (source or drain electrode). Our PEEM measurement provides clear evidence for these discussions and new findings on carrier transport in AATs. First, our study revealed the formation of a depletion layer at the lateral p–n junction in a specific V_G range ($V_{on} < V_G < V_{off}$), indicating that the lateral p–n junction serves as the dominant carrier-transport path. Another crucial part of this study is to provide insight into minority carrier conduction. Most electrons (minority carriers for the α-6T channel), which are transported from the PTCDI-C8 channel, recombine with the accumulated holes (major carriers) in the α-6T channel. This finding provides us new knowledge in addition to the transport mechanism proposed by Kim et al.[23] The same transport process can be considered for hole conduction.

3. Conclusion

We have achieved real-time visualization of conductive electrons in an organic AAT using an operando PEEM approach. This approach, combined with the analysis of transistor properties, revealed the detailed carrier-transport mechanism in AAT. The formation of a depletion layer at the lateral p–n junction, which was induced by the pinch-off states in the constituent channels, is particularly significant. The result shows that the steep potential gradient at the lateral p–n junction enhanced the electron conduction from the PTCDI-C8 to the α-6T channel. However, the vertical p–n junction was discovered to not work as an effective transport channel. These findings verify the importance of the lateral p–n junction for the NDT property. Furthermore, we show that the recombination of electrons occurs in the α-6T layer. Our results provide us with a better understanding of carrier transport in AATs, leading to further development of high-performance organic AATs.

4. Experimental Section

Formation of BG-AATs: BG and TC-AATs with α-6T and PTCDI-C8 layers were prepared on a highly doped p^+-Si (001) substrate with a 200-nm-thick SiO_2 layer using the vacuum thermal deposition approaches. First, a 30 nm-thick Au electrode was deposited on the SiO_2/Si substrate as a BG electrode. Subsequently, a 30 nm-thick HfO_2 film was grown as a BG insulating layer by an atomic layer deposition system. The substrate temperature was fixed at 175 °C. Tetrakis(dimethylamino)hafnium and water were used as hafnium and oxygen sources. Subsequently, a 20 nm-thick fluorocarbon polymer (CYTOP) (AGC chemicals, CTL-809M and SOLV-180) was spin-coated to passivate the carrier trap sites on the HfO_2 surface and facilitate the charge transport of the organic channels. Afterward, α-6T (10 nm) and PTCDI-C8 (15 nm) films were grown as n-type and p-type organic channels using a thermal vacuum deposition approach at a background pressure of 10^{-7} Pa. To form a p–n junction, the two organic layers were patterned through shadow masks with a partially overlapped region in the transistor channel. For the source and drain electrodes, 30-nm-thick Au films were then deposited using a thermal vacuum deposition system. The AAT's typical width and length were 400 and 200 µm, respectively.

Transistor Measurements: The transistor measurements of AATs were conducted using a semiconductor device analyzer (Agilent, B1500A) under atmospheric conditions prior to PEEM measurements. Furthermore, the transistor properties were examined under vacuum conditions under the PEEM measurements using a combined system of two DC voltage sources (Matsusada, P4K-80M and P4L-36) and two picoampere meters (ADCMT, 8240 and 5350). All the measurements were conducted at room temperature.

PEEM Measurements: The distribution of conductive electrons as a function of gate voltage was imaged by PEEM (Focus GmbH) with a photon energy tunable light source. The light source was composed of a femtosecond laser system (Light Conversion, Pharos SP) and an optical parametric amplifier (Light Conversion, Orpheus). The maximum

power, repetition rate, and pulse width of laser pulses ejected from Pharos SP were 300 µJ per pulse, 20 kHz, and 190 fs, respectively. All the photons were injected into Orpheus, and the maximum power was tuned to be below 25 µJ per pulse, and the wavelength was continuously tunable in the range of 620 (2.0 eV)–2500 nm (0.5 eV). The wavelength of output laser pulses from Orpheus was expanded to 220 nm (5.64 eV) using one or two nonlinear crystals (β-BaB_2O_4).[32,33] The fermi level of Au electrodes, LUMO and HOMO levels of α-6T, and LUMO level of PTCDI-C8 were estimated by taking photoelectron emission spectra using an energy filter for photoelectron kinetic energy with three excitation photon energies of 3.2, 4.8, and 5.6 eV (FOCUS GmbH, Imaging Energy Filter) (Figures S2 and S3, Supporting Information). The energy resolution was set to 100 meV. The spatial resolution was 100 nm at the current PEEM lens parameters.

Pump and probe experiments were conducted to estimate the HOMO level of PTCDI-C8 (Figure S2e, Supporting Information). The probe pulses to induce photoelectron emission from HOMO was the fourth harmonic generation of laser pulses (4.82 eV), which was a part of the photons not used for Orpheus' generation. The pump pulses were the wavelength tunable source mentioned above. The delay between pump and probe pulses was controlled using an optical delay stage and scanned from −2 to 4 ps for the current experiments. The temporal resolution was approximately 100 fs.

The sample plate for the PEEM was designed and manufactured to have 16 electric contacts with the sample (Figure 1c).

Image Processing and Statistical Analysis: All the PEEM images were saved as 12-bit TIFF files. To enhance the contrast of the detected images, as shown in Figure 3 and in the supporting media, we performed image processing with the following equation:

$$I_{conv} = \left[(I_{orignal} - I_{background})^{1.5} \right] \times 0.36 \quad (3)$$

where I_{conv}, $I_{orignal}$, and $I_{background}$ are the converted, original, and background pixel brightness values, respectively. The adjusted images were then converted to the JPEG format and denoised in a five-pixel square (1.2 µm × 1.2 µm) using a median filter.

The photoemission intensity profiles shown in Figure 4b,c were obtained from the original 12-bit TIFF images. The selected area was 950 pixels wide by 200 pixels high (actual scale: 230 µm × 50 µm; see Figure S8, Supporting Information). First, the pixel brightness values were averaged in the height direction of the selected area. The outliers, which were four-times larger than the averaged values, were replaced with the averaged values. Finally, a moving average of the neighboring 15 pixels was conducted at each pixel in the width direction of the selected area.

To statistically evaluate the transition voltages and the relative variation in the photoemission intensities of the PTCDI-C8 and α-6T regions as a function of V_G (Figures 4a), we executed the MCMC method with the PyMC package.[41] Here, the statistical analysis was conducted by dividing PTCDI-C8 into three sections and 6T into two sections for their respective V_G ranges. This was done because the photoemission intensities in the α-6T and PTCDI-C8 regions, which correspond to the red and blue line plots in Figure 4a, show stepwise increases: two-step increase for PTCDI-C8 and one-step increase for α-6T. The difference in the averaged photoemission intensities in the divided sections was confirmed with an accuracy of >99.5% for both constituent layers. The details of the statistical analyses are summarized in Figures S6 and S7 (Supporting Information).

Supporting Information

Supporting Information is available from the Wiley Online Library or from the author.

Acknowledgements

This research was supported by the World Premier International Center (WPI) for Materials Nanoarchitectonics (MANA) of the National Institute for Materials Science (NIMS), MEXT Q-LEAP ATTO grant number JPMXS0118068681, JST FOREST Program grant number JPMJFR203P, TIA Kakehashi grant number TK19-21, and JSPS Kakenhi grant numbers 19H00866, 21F21052, 17H06372, 21H01752 and 20H02808.

Conflict of Interest

The authors declare no conflict of interest.

Data Availability Statement

Research data are not shared.

Keywords

carrier transport, lateral p–n junctions, negative differential transconductance, organic antiambipolar transistors, photoemission electron microscopy

Received: February 8, 2022
Revised: May 25, 2022
Published online:

[1] Y. Wang, W.-X. Zhou, L. Huang, C. Xia, L.-M. Tang, H.-X. Deng, Y. Li, K.-Q. Chen, J. Li, Z. Wei, *2D Mater.* **2017**, *4*, 025097.
[2] A. Nourbakhsh, A. Zubair, M. S. Dresselhaus, T. Palacios, *Nano Lett.* **2016**, *16*, 1359.
[3] D. Jariwala, S. L. Howell, K.-S. Chen, J. Kang, V. K. Sangwan, S. A. Filippone, R. Turrisi, T. J. Marks, L. J. Lauhon, M. C. Hersam, *Nano Lett.* **2016**, *16*, 497.
[4] Y. Li, Y. Wang, L. Huang, X. Wang, X. Li, H.-X. Deng, Z. Wei, J. Li, *ACS Appl. Mater. Interfaces* **2016**, *8*, 15574.
[5] Z. Wang, X. He, X.-X. Zhang, H. N. Alshareef, *Adv. Mater.* **2016**, *28*, 9133.
[6] H. J. Park, C.-J. Park, J. Y. Kim, M. S. Kim, J. Kim, J. Joo, *ACS Appl. Mater. Interfaces* **2018**, *10*, 32556.
[7] H. Yoo, S. On, S. B. Lee, K. Cho, J.-J. Kim, *Adv. Mater.* **2019**, *31*, 1808265.
[8] Y. Wakayama, R. Hayakawa, *Adv. Funct. Mater.* **2019**, *30*, 1903724.
[9] D. Sarkar, X. Xie, W. Liu, W. Cao, J. Kang, Y. Gong, S. Kraemer, P. M. Ajayan, K. Banerjee, *Nature* **2015**, *526*, 91.
[10] A. W. Dey, J. Svensson, M. Ek, E. Lind, C. Thelander, L.-E. Wernersson, *Nano Lett.* **2013**, *13*, 5919.
[11] T. Roy, M. Tosun, X. Cao, H. Fang, D.-H. Lien, P. Zhao, Y.-Z. Chen, Y.-L. Chueh, J. Guo, A. Javey, *ACS Nano* **2015**, *9*, 2071.
[12] K. Maeda, N. Okabayashi, S. Kano, S. Takeshita, D. Tanaka, M. Sakamoto, T. Teranishi, Y. Majima, *ACS Nano* **2012**, *6*, 2798.
[13] Y. Takahashi, A. Fujiwara, K. Yamazaki, H. Namatsu, K. Kurihara, K. Murase, *Appl. Phys. Lett.* **2000**, *76*, 637.
[14] M. Huang, S. Li, Z. Zhang, X. Xiong, X. Li, Y. Wu, *Nat. Nanotech.* **2017**, *12*, 1148.
[15] C. R. P. Inbaraj, R. J. Mathew, R. K. Ulaganathan, R. Sankar, M. Kataria, H. Y. Lin, Y.-T. Chen, M. Hofmann, C.-H. Lee, Y.-F. Chen, *ACS Nano* **2021**, *15*, 8686.
[16] K.-H. Kim, H.-Y. Park, J. Shim, G. Shin, M. Andreev, J. Koo, G. Yoo, K. Jung, K. Heo, Y. Lee, H.-Y. Yu, K. R. Kim, J. H. Cho, S. Lee, J.-H. Park, *Nanoscale Horiz.* **2020**, *5*, 654.
[17] J. Yi, X. Sun, C. Zhu, S. Li, Y. Liu, X. Zhu, W. You, D. Liang, Q. Shuai, Y. Wu, D. Li, A. Pan, *Adv. Mater.* **2021**, *33*, 2101036.
[18] K. Kobashi, R. Hayakawa, T. Chikyow, Y. Wakayama, *Adv. Electron. Mater.* **2017**, *3*, 1700106.

[19] K. Kobashi, R. Hayakawa, T. Chikyow, Y. Wakayama, *ACS Appl. Mater. Interfaces* **2018**, *10*, 2762.
[20] K. Kobashi, R. Hayakawa, T. Chikyow, Y. Wakayama, *J. Phys. Chem. C* **2018**, *122*, 6943.
[21] K. Kobashi, R. Hayakawa, T. Chikyow, Y. Wakayama, *Nano Lett.* **2018**, *18*, 4355.
[22] C.-H. Kim, R. Hayakawa, Y. Wakayama, *Adv. Electron. Mater.* **2020**, *6*, 1901200.
[23] C.-H. Kim, H. Yoo, *Adv. Electron. Mater.* **2021**, *7*, 2100167.
[24] S.-W. Jo, J. Choi, R. Hayakawa, Y. Wakayama, S. Hung, C.-H. Kim, *J. Mater. Chem. C* **2021**, *9*, 15415.
[25] H. Yoo, C.-H. Kim, *IEEE Electron Device Lett.* **2021**, *42*, 1323.
[26] D. Panigrahi, R. Hayakawa, K. Fuchii, Y. Yamada, Y. Wakayama, *Adv. Electron. Mater.* **2021**, *7*, 2000940.
[27] D. Panigrahi, R. Hayakawa, K. Honma, K. Kanai, Y. Wakayama, *Appl. Phys. Express* **2021**, *14*, 081004.
[28] C. Lee, J. Choi, H. Park, C. Lee, C.-H. Kim, H. Yoo, S. G. Im, *Small* **2021**, *17*, 2103365.
[29] K. Fukumoto, Y. Yamada, K. Onda, S. Koshihara, *Appl. Phys. Lett.* **2014**, *104*, 053117.
[30] K. Fukumoto, K. Onda, Y. Yamada, T. Matsuki, T. Mukuta, S. Tanaka, S. Koshihara, *Rev. Sci. Instrum.* **2014**, *85*, 083705.
[31] M. Iwasawa, R. Tsuruta, Y. Nakayama, M. Sasaki, T. Hosokai, S. Lee, K. Fukumoto, Y. Yamada, *J. Phys. Chem. C* **2020**, *124*, 13572.
[32] K. Fukumoto, Y. Suzuki, S. Hou, M. D. Birowosuto, A. Jaffre, D. Alamarguy, E. H. T. Teo, H. Wang, B. K. Tay, M. Boutchich, *J. Phys. D: Appl. Phys.* **2020**, *53*, 405106.
[33] Y. Fukami, M. Iwasawa, M. Sasaki, T. Hosokai, H. Nakanotani, C. Adachi, K. Fukumoto, Y. Yamada, *Adv. Optical Mater.* **2021**, *9*, 2100619.
[34] K. Akaike, N. Koch, G. Heimel, M. Oehzelt, *Adv. Mater. Interfaces* **2015**, *2*, 1500232.
[35] C.-H. Kim, I. Kymissisc, *J. Mater. Chem. C* **2017**, *5*, 4598.
[36] N. Hiroshiba, R. Hayakawa, T. Chikyow, Y. Yamashita, H. Yoshikawa, K. Kobayashi, K. Morimoto, K. Matsuishi, Y. Wakayama, *Phys. Chem. Chem. Phys.* **2011**, *13*, 6280.
[37] A. Wan, J. Hwang, F. Amy, A. Kahn, *Org. Electron.* **2005**, *6*, 47.
[38] Y. Tanaka, K. Ikegami, T. Maruyama, H. Kinjo, H. Ishii, *Appl. Phys. Express* **2018**, *11*, 081601.
[39] M. Ando, S. Heike, M. Kawasaki, T. Hashizume, *Appl. Phys. Lett.* **2014**, *105*, 193303.
[40] L. Bürgi, H. Sirringhaus, R. H. Friend, *Appl. Phys. Lett.* **2002**, *80*, 2913.
[41] C. Davidson-Pilon, *Bayesian Methods for Hackers: Probabilistic Programming and Bayesian Inference*, Addison-Wesley, Boston, MA, USA **2015**.
[42] S. D. Vusser, S. Schols, S. Steudel, S. Verlaak, J. Genoe, W. D. Oosterbaan, L. Lutsen, D. Vanderzande, P. Heremans, *Appl. Phys. Lett.* **2006**, *89*, 223504.